ON THE RADIAL ONSET OF CLUMPING IN THE WIND OF THE B0I MASSIVE STAR QV NOR

The Astrophysical Journal, 810:102 (11pp), 2015 September 10 doi:10.1088/0004-637X/810/2/102

ON THE RADIAL ONSET OF CLUMPING IN THE WIND OF THE B0I MASSIVE STAR QV NOR

J. M. Torrejón[1], N. S. Schulz[2], M. A. Nowak[2], L. Oskinova[3], J. J. Rodes-Roca[1], T. Shenar[3], and J. Wilms[4]
[1] Instituto Universitario de Física Aplicada a las Ciencias y las Tecnologías, Universidad de Alicante, E-03080 Alicante, Spain; jmt@ua.es
[2] MIT Kavli Institute for Astrophysics and Space Research, Cambridge, MA 02139, USA
[3] Institut für Physik und Astronomie, Universität Potsdam, Karl-Liebknecht-Str. 24/25, D-14476 Potsdam, Germany
[4] Dr. Karl Remeis Sternwarte & ECAP, Universität Erlangen-Nüremberg, Bamberg, Germany
Received 2015 May 20; accepted 2015 July 29; published 2015 September 3

ABSTRACT

We present an analysis of a 78 ks *Chandra* high-energy transmission gratings observation of the B0I star QV Nor, the massive donor of the wind-accreting pulsar 4U1538−52. The neutron star (NS) orbits its companion in a very close orbit ($r < 1.4R_*$, in units of the stellar radii), thereby allowing probing of the innermost wind regions. The flux of the Fe Kα line during eclipse reduces to only ∼30% of the flux measured out of eclipse. This indicates that the majority of Fe fluorescence must be produced in regions close to the NS, at distances smaller than $1R_*$ from its surface. The fact that the flux of the continuum decreases to only ∼3% during eclipse allows for a high contrast of the Fe Kα line fluorescence during eclipse. The line is not resolved and centered at $\lambda = 1.9368^{+0.0032}_{-0.0018}$ Å. From the inferred plasma speed limit of $v < c\frac{\Delta\lambda}{\lambda} < 800\,\mathrm{km\,s^{-1}}$ and range of ionization parameters of $\log \xi = [-1, 2]$, together with the stellar density profile, we constrain the location of the cold, dense material in the stellar wind of QV Nor using simple geometrical considerations. We then use the Fe Kα line fluorescence as a tracer of wind clumps and determine that these clumps in the stellar wind of QV Nor (B0I) must already be present at radii $r < 1.25R_*$, close to the photosphere of the star.

Key words: stars: individual (QV Nor, 4U1538+52) – stars: winds, outflows – X-rays: binaries

1. INTRODUCTION

The classical theory of radiatively driven stellar winds predicts the average wind properties with good precision (Castor et al. 1975, CAK). However, it was envisaged early on that the stellar winds are unlikely to be steady (Lucy & Solomon 1970). MacGregor et al. (1979 and the references therein) found that the radiatively driven stellar winds are unstable, and that the velocity perturbations become strongly amplified in the supersonic parts of the wind. Lucy & White (1980) conjectured that a wind breaks up into a population of blobs that are confined by an ambient gas. The subsequent radiation-hydrodynamic simulations revealed that strong shocks develop in the wind, leading to strong inhomogeneous density and velocity distributions on small scales (Owocki et al. 1988; Feldmeier 1995). These and other modeling works are supported by a plethora of observational evidence (e.g., Ebbets 1982; Kaper et al. 1996; Eversberg et al. 1998; Massa et al. 2003; Oskinova et al. 2006; Lépine & Moffat 2008; Zsargó et al. 2008).

Although the clumpy wind paradigm was well-established from the beginning of stellar wind studies, it has been recognized only relatively recently that clumping has very important implications for the empirical diagnostics of key stellar wind parameters, such as mass-loss rates. Assuming optically thin clumps ("microclumping") in the analysis of UV spectra leads to the reduction of empirical mass-loss rates by an order of magnitude or even more (Bouret et al. 2005; Fullerton et al. 2006). On the other hand, allowing for optically thick clumping ("macroclumping") in the analysis of UV spectra results in mass-loss rates that agree well with the predictions of the CAK theory (Oskinova et al. 2007; Surlan et al. 2013; Shenar et al. 2015). Clumping is also important in the winds of B-type supergiants and should be accounted for in the estimates of the B-supergiant mass-loss rates (Prinja & Massa 2010, 2013). Although accurate knowledge of mass-loss rates has far-reaching implications for our understanding of massive star evolution and stellar feedback (see, e.g., Hamann et al. 2008 for a comprehensive review), the physical properties of these clumps, such as their sizes, density, and spatial distribution, are poorly known. This is largely due to the lack of proper observational constraints (Oskinova et al. 2012).

Of special interest is the radial onset of stellar wind clumping. Wind simulations predict that close to the stellar photosphere, the wind is relatively smooth, and the strong instabilities develop at about $\sim 1.5R_*$, i.e., at the distances where the wind has already reached a significant fraction of its terminal velocity v_∞ (e.g., Feldmeier et al. 1997). On the other hand, from empirical studies it emerges that the innermost wind regions are significantly clumped and strong shocks and magnetic fields may be present. (Puls et al. 2006; Waldron & Cassinelly 2007). One of the models developed to accommodate these finding suggests that sub-surface convection may play a role in massive stars, resulting in surface magnetic spots and causing the clumping to already originate at the photosphere (Cantiello & Braithwaite 2011).

In high-mass X-ray binaries (HMXBs) a compact object, a neutron star (NS), or a black hole, orbits the massive star deeply embedded into its wind. The copious X-rays produced via wind accretion provide an excellent source of X-ray illumination. One of the primary tools for studying the regions of high density in stellar winds is the fluorescence Kα line from near-neutral Fe (Torrejón et al. 2010; Giménez-García et al. 2015). The ionization parameter $\xi = L_X/[n(r_X)r_X^2]$, where $n(r_X)$ is the number density of atoms at radial distance r_X from the X-ray source, must be below some $10^2\,\mathrm{erg\,cm\,s^{-1}}$, at most, to keep the Fe at low levels of ionization. For typical luminosities of the order of $L_X \approx 10^{36}\,\mathrm{erg\,s^{-1}}$ and distances of 10^{11-12} cm, the particle densities must be $10^{10-12}\,\mathrm{cm^{-3}}$, which is a factor between 1 and 100 larger than the average wind

densities given by the smooth wind scenario. In other words, the Fe Kα fluorescence line is a tracer of the wind clumps.

In this paper we aim to study the radial location of clumps of QV Nor , the B0 supergiant donor of the X-ray source 4U1538 −52 . We proposed to observe this unique system because of a number of characteristics. (1) The system is eclipsing. This allows us to disentangle the amount of Fe Kα emission produced close to the X-ray source from that produced further out in the wind. (2) The NS orbits QV Nor in a 3.7 d orbit at radial distances from the donor star, ranging from $r \sim 1.35R_*$ to $\lesssim 1.5R_*$, allowing probing of the innermost wind region of a B0I star. Two orbital solutions are possible (Clark 2000; Baykal et al. 2006; Mukherjee et al. 2006) and both can individually be precisely determined. (3) The periastron passage is very close to the eclipse, allowing probing of the innermost wind with a maximum contrast between the emission lines and the continuum. (4) The wind density profile has been studied in detail and is well-established (Clark et al. 1994, using *ASCA*; CWN94 henceforth). This will allow us to use the observed properties of the Fe Kα line to accurately constrain its production site.

2. OBSERVATIONS

We observed QV Nor with *Chandra* in two runs carried out during 2014 February 3 and 6, respectively, corresponding to ObsIDs 15704 (eclipse) and ObsID 16581 (-eclipse and eclipse ingress). The High Energy Transmission Gratings spectrometer (HETG; Canizares et al. 2005) acquired data during a total of 77.90 ks. There are two sets of gratings available, the High Energy Grating (HEG), which offers a resolution of 0.011 Å in the the bandpass of about 1.5–16 Å, and the Medium Energy Grating (MEG) which offers a resolution of 0.021 Å in the the bandpass of about 1.8–31 Å. Our observations provided significant data in the range between 1.7 and 12 Å. The spectra and the response files (`arf` and `rmf`) were extracted using standard procedures with the CIAO software (v 4.4). First dispersion orders ($m = \pm 1$) were fitted simultaneously. The peak source flux both at HEG and MEG gratings is $\approx 5.4 \times 10^{-10}$ erg s^{-1} cm^{-2}, roughly 5 times lower than the level at which pileup starts to be important.[5] The analysis was performed with the Interactive Spectral Interpretation System (ISIS) v 1.6.1-24 (Houck & Denicola 2000).

3. LIGHT CURVE ANALYSIS

In Figure 1 we show the 1.5–4 Å and 4–15 Å light curves, respectively, for ObsID 16581 binned in 526 s intervals. The integrated fluxes in these bands are denominated as *H* and *S*, respectively. We define the *out-of-eclipse* (*O*) time from 0 to 36 ks, which corresponds to the mid-orbital phase $\phi = 0.77$ using the ephemeris of Clark (2000). The interval from 36 to 42 ks is defined as *eclipse ingress* (*I*), corresponding to the mid-orbital phase $\phi = 0.88$. From this time on, plus ObsID 15704 (not shown), is defined as *eclipse* (*E*, mid-orbital phase $\phi = 0.97$). Both observations combined cover nearly one quarter of the NS orbit, from quadrature ($\phi = 0.75$) to mid-eclipse ($\phi = 0.0$). The eclipse starts in the soft band around $t = 22$ ks, that is, about 14 ks earlier than in the hard band. The (red) diamonds depict the hardness ratio $HR = (H - S)/(H + S)$. Clearly, the *HR* is anti-correlated with the flux in both bands, i.e., the source is softer when brighter and vice versa.

In the left panel of Figure 4 we show the Lomb–Scargle periodogram of the *Chandra* HETG light curve binned to 5 s intervals. It clearly shows the NS spin period at $P = 526.69 \pm 1.31$ s, with no discernible period difference between the *H* and the *S* bands. The right panel shows the NS spin pulse folded at this period. As can be seen, the light curve

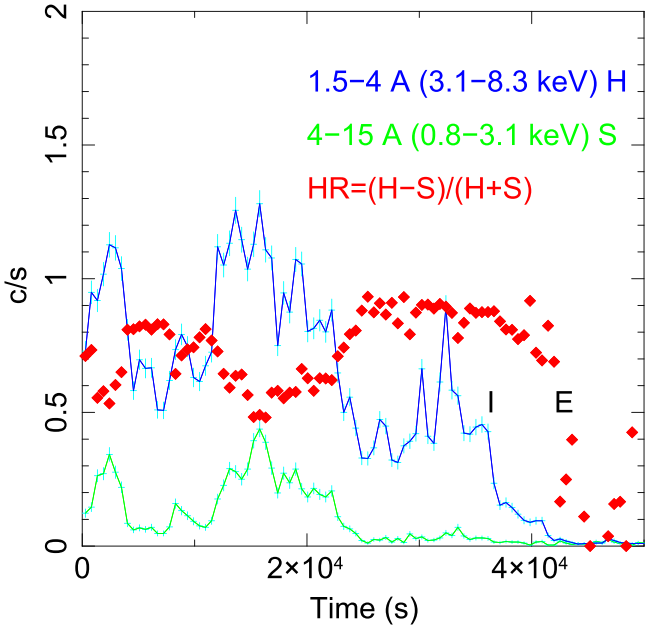

Figure 1. *Chandra* light curve, in the 1.6–15 Å wavelength range corresponding to ObsID 16581, grouped into 526 s bins. We define the *out of eclipse* (*O*) phase from 0 to 36 ks, which corresponds to the orbital phase $\phi = 0.77$. The orbital phase from 36 to 42 ks is defined as *eclipse ingress* (*I*) ($\phi = 0.88$). The orbital phase from 42 to 52 ks, together with the ObsID 15704, corresponds to *eclipse* (*E*) ($\phi = 0.97$). The start times of ingress and eclipse are marked with *I* and *E*, respectively. The blue and green lines represent the data in the Hard and Soft bands. The error bars are displayed in light blue.

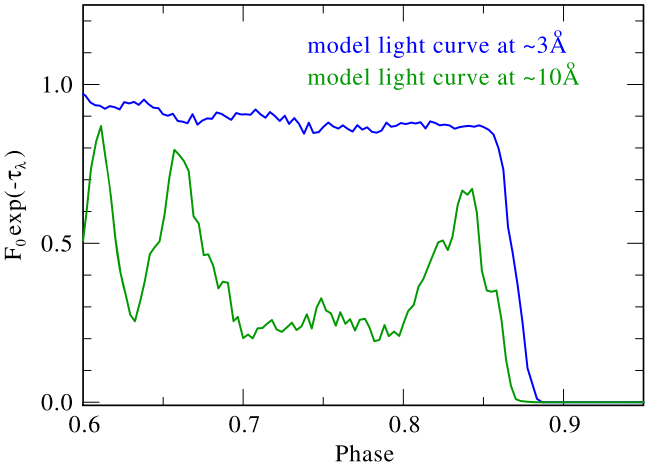

Figure 2. Monochromatic synthetic X-ray light curves at $\lambda = 3$ and λ=10 Å , approximating the bands shown in Figure 11. The synthetic light curves are for one realization of our stochastic wind model consisting of 1.8×10^4 clumps (see the text for details). The horizontal axis shows the binary phase with the X-ray eclipse at phase 1. The vertical axis shows the wind transmission for X-rays, normalized such that in the absence of any wind absorption the monochromatic flux $F_0 \equiv 1$.

[5] See *The Chandra ABC Guide to Pileup*, v.2.2, http://cxc.harvard.edu/ciao/download/doc/pileup-abc.pdf.

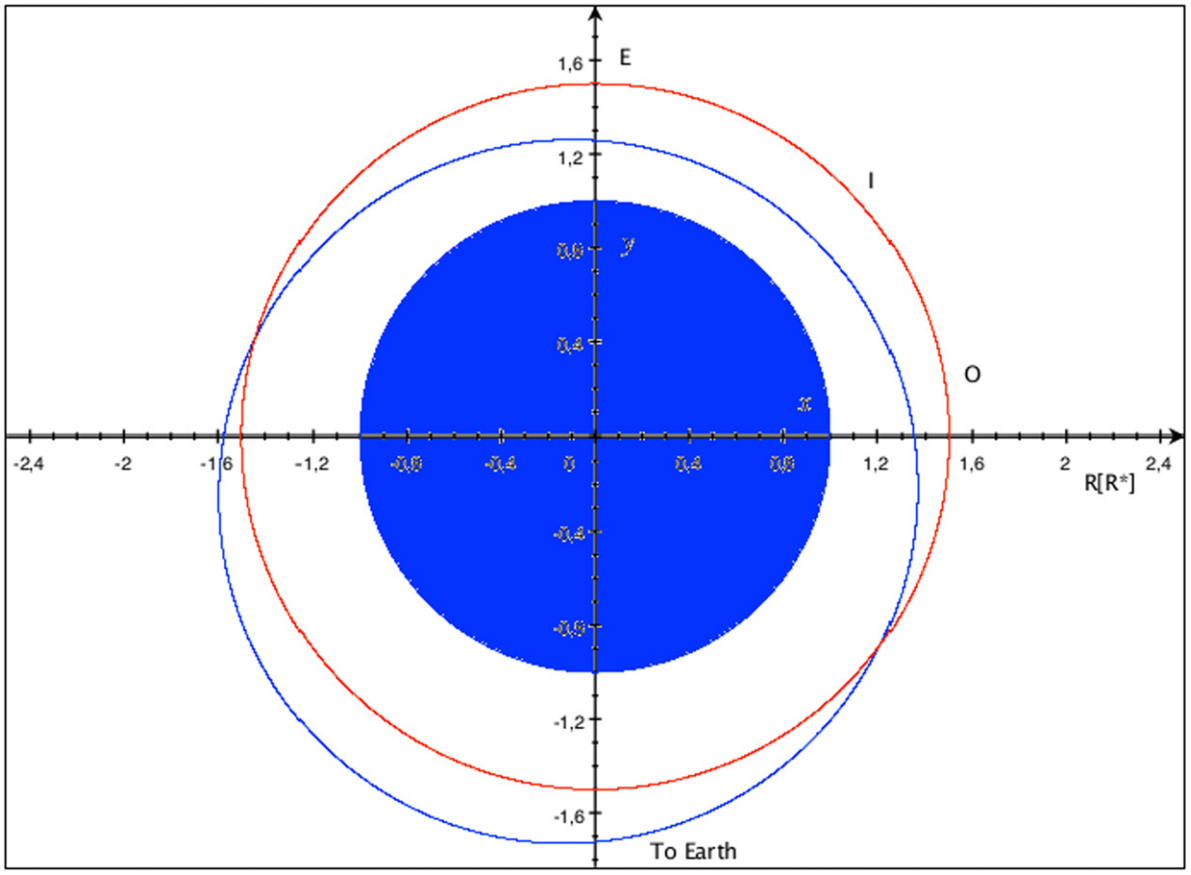

Figure 3. Sketch of the binary system. The star's core is the filled blue circle. The two possible orbits of the NS are the red circle ($e = 0$ solution) and the blue circle ($e = 0.174$ solution). The *Chandra* observation covers three orbital phases: *O* (out of eclipse), *I* (eclipse ingress), and *E* (eclipse). For the eccentric orbit, during the eclipse observation (*E*), the NS is at $1.35R_*$ while during the out-of-eclipse (*O*) observation it was at $1.4R_*$. In the circular solution the NS is always at $1.5R_*$.

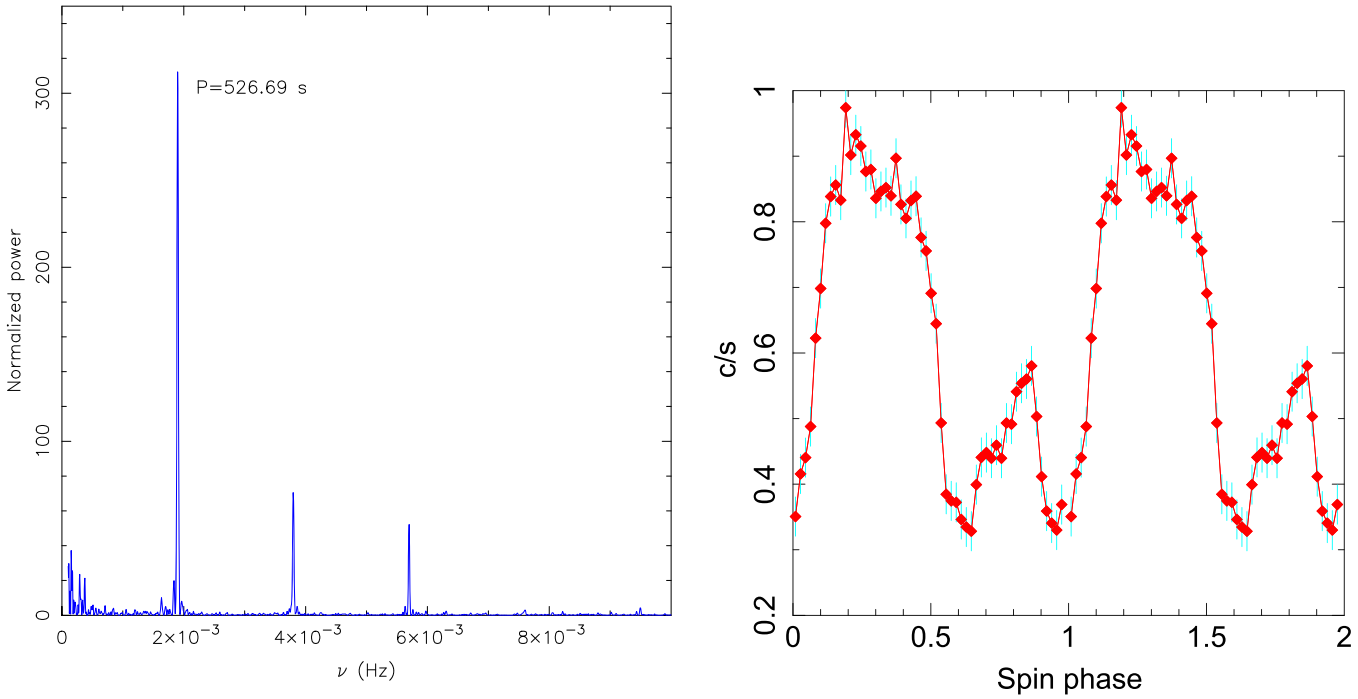

Figure 4. Left: Lomb–Scargle periodogram of the *Chandra* high-energy (1.5–4 Å) light curve rebinned to 5 s intervals. The main peak corresponds to an NS spin period of $P = 526.69 \pm 1.31$ s consistent with the spin-down trend of the pulsar. The first two harmonics are also clearly seen. Right: the light curve folded into the NS spin period. Two periods are shown for clarity.

shows a double peak and is strongly modulated, with a pulsed fraction[6] of ∼54%. In order to minimize the modulation effect due to the NS spin in Figure 1 we have binned the whole light curve into 526 s bins. The observed light curves *S* and *H* show significant variability from bin to bin and and along the whole observation. This is quite common among HMXBs with NSs orbiting their donor stars at larger distances that in QV Nor. The high-energy band is much less sensitive to absorption effects. In order to check the possible influence of absorption by the donor's wind and/or intrinsic variability of the source, we produced synthetic X-ray light curves using our two-dimensional (2D) stochastic wind code (Oskinova et al. 2004). The model describes, in a generic way, the structures and physical conditions of the stellar wind. It is assumed that the flow is spherically symmetric and stationary in a statistical sense. All the wind material is condensed into a finite number of discrete clumps that propagate in radial directions. The stellar mass-loss rate and the radial optical depth are conserved. Thus, in addition to the typical wind parameters, $\dot{M}$ and v_∞, we introduce a new one called fragmentation frequency, n_0 (s^{-1}), that determines the total number of clumps in each radial direction. In addition, the model allows for different shapes of wind clumps such that the clump optical depth for X-rays may depend on orientation.

For the simulations we used the stellar wind parameters of QV Nor. The source of X-rays is located between 1.3 R_* and 1.5 R_*. We assume that the X-ray source is constant, i.e., that the accretion rate onto the NS is constant. The X-rays propagate toward the observer and suffer from absorption in the stellar wind. To realistically estimate the wind absorption, we adopted $\dot{M} = 10^{-6}\ M_\odot\ \mathrm{yr}^1$ and a wind with a standard β-law velocity with $\beta = 0.8$ and $v_\infty = 1900\ \mathrm{km\ s}^{-1}$. The wind mass-absorption coefficients were adopted according to our NLTE stellar wind models of OB-(super)giants (e.g., Shenar et al. 2015), i.e., at $\lambda \approx 10$ Å, $\kappa = 20\ \mathrm{cm}^2\ \mathrm{g}^{-1}$ while at $\lambda \approx 3$ Å, $\kappa = 3\ \mathrm{cm}^2\ \mathrm{g}^{-1}$.

As a first step we simulated a smooth, unclumped wind and computed the model X-ray light curves. They significantly differ from the observed ones and consequently we do not consider them any further. As a next step, we computed a small grid of model light curves for different fragmentation frequencies and clump shapes and compared them with the observed light curves. We show in Figure 2 those synthetic light curves that empirically resemble the observed ones. Three conclusions can be drawn from the comparison. The first, most robust conclusion is that a smooth wind and a stationary accretion rate onto the NS can be excluded. This is in agreement with our analysis of Fe fluorescent lines (see below). The second conclusion is that the variability observed in the hard band cannot solely be explained by absorption in the clumped stellar wind. The wind is largely transparent for radiation with $\lambda < 4$ Å. The variability observed in the hard band of QV Nor implies a non-stationary accretion rate. The third conclusion is that absorption in a clumped stellar wind may help to explain the variability of the light curve in the soft band provided that the wind is significantly clumped. Also, our simulations point out that some larger-scale structures may be present in the wind, such as, e.g., wakes. Overall, the analysis of light curves confirms that the wind in QV Nor must be significantly structured already close to the stellar photosphere.

[6] Defined as $PF = F_{\max} - F_{\min}/F_{\max} + F_{\min}$ and using the corresponding fluxes given in Figure 4.

In Figure 3 we present a sketch of the system with the two possible orbital solutions proposed by Clark (2000) based on *RXTE* data. The blue filled circle is the stellar core. The open blue and red circles are the orbital solutions for the eccentricities $e = 0.174$ and $e = 0$, respectively. The beginnings of the three orbital phases observed are indicated with the letters *O*, *I,* and *E* respectively. Mukherjee et al. (2006) argue in favor of the eccentric orbit. However, Rawls et al. (2011), point out that both solutions are still compatible with the data. Therefore, the exact form of the orbit is still an open issue. In any of the two cases, however, the NS orbits QV Nor at possible radial distances ranging from $1.35R_*$ to $1.5R_*$ at maximum, thereby probing the innermost wind region.

4. SPECTRAL ANALYSIS

4.1. Continuum Models

In order to properly study the emission lines we need a good model of the underlying continuum. Models that can self-consistently describe the spectral continuum of X-ray pulsars in HMXBs do not yet exist, so we use phenomenological models instead. The model suggested by Rodes-Roca et al. (2011) consists of three power laws with the same photon index but different normalizations and absorption columns. Another model by Hemphill et al. (2014) applies partial coverage absorption of an exponentially cutoff single power law. Since we are mostly concerned with emission lines we chose the latter because it requires less free parameters. The emission lines are well-described using either of the continuum models. Since the upper limit of the *Chandra* bandpass (∼9 keV) is well below the reported cutoff energy (∼21 keV), the model used gives the flux $F(E)$ at a given energy E as a simple power law

$$F(E) = \mathrm{Abs}(E) \times C_{\mathrm{po}} \times E^{-\Gamma}, \quad (1)$$

where C_{po} is the power-law normalization constant and Γ is the photon index. The absorption is modeled with a partial covering absorber of the form

$$\mathrm{Abs}(E) = (1 - f) * \mathrm{TB}_{\mathrm{new}_1}(E) + f * \mathrm{TB}_{\mathrm{new}_2}(E), \quad (2)$$

where the photoelectric absorption is modeled through `TBnew` (Wilms et al. 2010)[7] using the standard elemental abundances of Wilms et al. (2000) and the cross sections of Verner et al. (1996). f is the covering fraction that can be regarded as a proxy of the degree of clumpiness in the stellar wind. The density column N_{H}^2 associated with the photoelectric absorption,$\mathrm{TB}_{\mathrm{new}_2}$, thus describes the total absorption by wind clumps, covering a fraction f of the X-ray source, plus the interstellar medium (ISM) contribution. That is to say $N_{\mathrm{H}}^2 = N_{\mathrm{H}}^{\mathrm{clumps}} + N_{\mathrm{H}}^{\mathrm{ISM}}$. Likewise, N_{H}^1, associated with $\mathrm{TB}_{\mathrm{new}_1}$, describes the inter-clump medium absorption plus the interstellar medium absorption toward the star, $N_{\mathrm{H}}^1 = N_{\mathrm{H}}^{\text{inter-clump}} + N_{\mathrm{H}}^{\mathrm{ISM}}$, both contributing with a $(1 - f)$ fraction.

This model describes the continuum very well except for the longest wavelengths, beyond ∼9.5 Å ($E \leqslant 1.36$ keV), where a clear excess remains. This soft excess is a well-known feature of the HMXBs (Hickox et al. 2004) and its nature remains

[7] http://pulsar.sternwarte.uni-erlangen.de/wilms/research/tbabs

Table 1
Observations Journal

ObsID	Date	t_{exp}(ks)	ϕ (start)
15704	2014 Feb 03 10:27:14	25.63	0.97
16581	2014 Feb 06 10:21:40	52.27	0.77

mysterious. We can model the excess by adding the term

$$+\mathrm{TB}_{\mathrm{new_3}}(E) \times C_{\mathrm{bb}} \times E^3 \exp\left(-\frac{E}{kT_{\mathrm{bb}}}\right) \quad (3)$$

to Equation (1). The blackbody has a normalization C_{bb} and is modified by its own absorbing column $\mathrm{TB}_{\mathrm{new_3}}$. The temperature of this component has been fixed in the ingress (*I*) phase, while the normalization has been left free to vary. The excess, on the other hand, has not been detected during the eclipse (*E*). In general this excess appears to be quite peculiar. When it appears it requires a lower and independent column, which is lower than the one required in Equation (2). This excess has been seen in the *XMM-Newton* PN data of QV Nor (Rodes-Roca et al. 2011) and in Vela X-1 (Martinez-Núñez et al. 2014).

The large covering fraction ($f \lessapprox 1$) is consistent with the NS deeply embedded into the wind of QV Nor . The N_{H}^1 decreases from a value of $5.1^{+1.1}_{-1.2} \times 10^{22}\,\mathrm{cm}^{-2}$ out-of-eclipse to $1.6^{+0.9}_{-0.8} \times 10^{22}\,\mathrm{cm}^{-2}$ during eclipse. The latter value is compatible with the ISM absorption toward QV Nor deduced from the optical reddening $E(B-V) = 2.2$ (Crampton et al. 1978) which implies $N_{\mathrm{H}}^{\mathrm{ISM}} \sim 1.5 \times 10^{22}\,\mathrm{cm}^{-2}$. During the eclipse we do not see the X-ray continuum source (the NS) but, rather, its reflected (scattered) component through the donor's wind. The fact that $N_{\mathrm{H}}^1 = N_{\mathrm{H}}^{\text{inter-clump}} + N_{\mathrm{H}}^{\mathrm{ISM}} \approx N_{\mathrm{H}}^{\mathrm{ISM}}$ during phase *E* implies that the inter-clump medium contributes very little to the total absorption. On the other hand, N_{H}^1 is larger during phases *O* ($5.1 \times 10^{22}\,\mathrm{cm}^{-2}$) and *I* ($2.5 \times 10^{22}$ cm^{-2}). If we subtract the ISM contribution to these quantities, there is still an extra $3.6 \times 10^{22}\,\mathrm{cm}^{-2}$ and 0.9×10^{22} 3.6×10^{22} for phases *O* and *I*, respectively. This can be attributed to a density enhancement (a wake) trailing the NS. Such density enhancement in QV Nor has been already hypothesized (Mukherjee et al. 2006; Rodes-Roca et al. 2015). At orbital phase *O* the NS is almost at quadrature and therefore this trailing material would be straight between the NS and the observer.

The N_{H}^2, in turn, is mostly local absorption, attributable to the stellar wind clumps. Subtracting the ISM contribution, it increases from $\sim 11.2 \times 10^{22}\,\mathrm{cm}^{-2}$ out of eclipse up to $\sim 56.4 \times 10^{22}\,\mathrm{cm}^{-2}$ during eclipse.

The unabsorbed continuum flux during eclipse is $F_E \approx 0.03 F_O$. For a distance of 6.4 ± 1 kpc (Reynolds et al. 1992) the luminosity of QV Nor during our observation was $L_{\mathrm{X}} = (2.9 \pm 0.5) \times 10^{36}\,\mathrm{erg\,s}^{-1}$ and $(5 \pm 3) \times 10^{34}\,\mathrm{erg\,s}^{-1}$ for the *O* and *E* phases, respectively.

4.2. Emission Lines

In Figure 5, we show the *Chandra* HETG spectrum of QV Nor in the region 5.9–8.6 Å where a number of emission lines can be seen both out of eclipse and in eclipse (right panel). Our *Chandra* observation thereby confirms the tentative detection of emission lines made with *XMM-Newton* PN and MOS[8] (Rodes-Roca et al. 2011). In what follows we analyze the high-resolution spectrum and its line emissions.

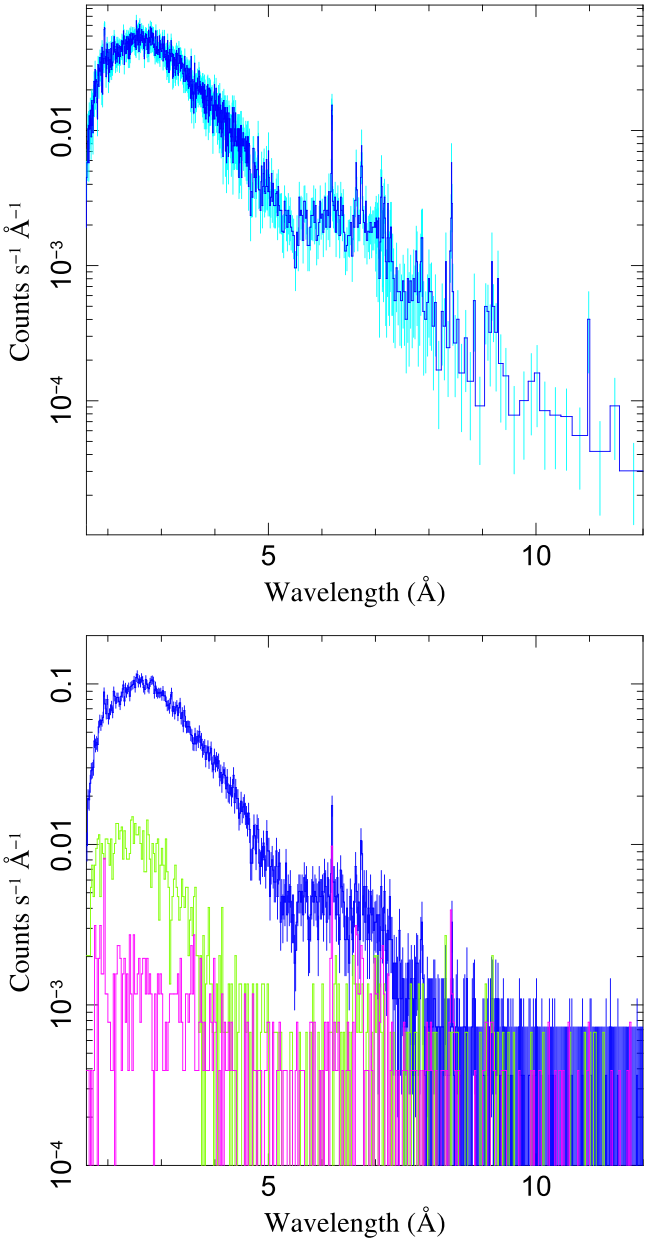

Figure 5. Top panel, the phase average spectrum. The contribution of the photoionized wind at long wavelengths is clearly seen. Bottom panel: the three orbital phases covered by this study $\phi = 0.77$ (eclipse; dark blue), $\phi = 0.88$ (Ingress; green), and $\phi = 0.97$ (Eclipse; magenta).

4.2.1. The Si XIII and Mg XI He Like Triplets

Within the available uncertainties, the fluxes shown by all elements other than Fe were similar in and out of eclipse. Therefore, in order to increase the signal-to-noise ratio (S/N) and better constrain the errors, we have fitted the emission lines with Gaussians for the orbital phase-averaged spectrum. The parameters are given in Table 3.

[8] The available *XMM-Newton RGS* spectrum is not usable because of its insufficient S/N due to the moderate absorption.

Table 2
Model Parameters for the Continuum

ϕ	$N_{\rm H}^{1}$ [a]	$N_{\rm H}^{2}$	f	$C_{\rm po}$ [b]	Γ	$N_{\rm H}^{3}$	$C_{\rm bb}$	$kT_{\rm bb}$	Flux[c]	χ_r^2 (dof)
0.77 (O)	$5.1^{+1.1}_{-1.2}$	$12.8^{+1.9}_{-1.4}$	$0.77^{+0.15}_{-0.04}$	$4.5^{+1.3}_{-0.8}$	$1.33^{+0.17}_{-0.15}$	$2.45^{+0.9}_{-0.8}$	$0.3^{+0.1}_{-0.1}$	$0.10^{+0.03}_{-0.02}$	$5.86^{+0.43}_{-0.27}$	0.92 (412)
0.88 (I)	$2.5^{+0.5}_{-0.5}$	$26.1^{+4.4}_{-4.2}$	$0.95^{+0.01}_{-0.05}$	$0.79^{+0.22}_{-0.14}$	1.33 (fixed)	$1.4^{+0.8}_{-0.7}$	$0.2^{+0.1}_{-0.1}$	0.10 (fixed)	$2.51^{+0.23}_{-0.15}$	0.95 (340)
0.97 (E)	$1.6^{+0.9}_{-0.8}$	58^{+10}_{-8}	$0.89^{+0.08}_{-0.09}$	$0.120^{+0.020}_{-0.018}$	1.33 (fixed)	...	...	...	$0.12^{+0.02}_{-0.02}$	0.95 (343)

Notes.
[a] All $N_{\rm H}$ in units of $\times 10^{22}$ cm^{-2}.
[b] All C in units of $\times 10^{-2}$.
[c] Unabsorbed 1–10 keV *model* flux in units of $\times 10^{-10}$ erg s^{-1} cm^{-2}.

Table 3
Emission Lines Identified in the *Chandra* Phase-averaged Spectrum of QV Nor

Ion	λ (Å)	Flux $\times 10^{-4}$ (ph s^{-1} cm^{-2})	σ (Å)
Si XIV Lyα	$6.1880^{+0.0019}_{-0.0017}$	$2.2^{+0.08}_{-0.06}$	0.005
Si XIII r	6.6396	$1.8^{+1.0}_{-0.6}$	0.005
Si XIII i	6.6850	<0.75	0.005
Si XIII f	6.7377	$1.8^{+1.0}_{-0.7}$	0.005
Si Kα	$7.1186^{+0.0005}_{-0.0010}$	$1.0^{+1.8}_{-0.5}$	0.005
Mg XII Lyα	8.4236 ± 0.0032	10^{+13}_{-5}	$0.009^{+0.009}_{-0.005}$
Mg XI r	9.1688	1.2 ± 0.7	0.005
Mg XI i	9.2300	<0.6	0.005
Mg XI f	9.3136	1.5 ± 0.7	0.005

Note. Numbers without errors are fixed to the quoted value.

The Si XIII He-like triplet at ~6.7 Å is clearly detected. In Figure 6 we show it as observed both out of eclipse (left) and during eclipse (right). The most conspicuous feature in both phases is the relative weakness of the *intercombination* (i) transition ($\lambda_i = 6.6850$ Å) and a dominance of the *resonance* (r, $\lambda_r = 6.6434$ Å) and *forbidden* (f; $\lambda_f = 6.7377$ Å) lines. This shows that the UV photospheric field is *not* important at the line production site since it effectively depopulates the f line into the i line and tends to *decrease* the f/i ratio (Porquet & Dubau 2000). Dominating r and f lines are also observed in the ionized B0I stellar wind in Vela X-1, both in the *Chandra* spectrum during eclipse (Schulz et al. 2002) and in the *ASCA* spectrum (Watanabe et al. 2006).

In order to check the significance of the i transition we have adopted a non-parametric approach and have compared the unbinned cumulative empirical distribution function of detected photons versus energy against two continuum functions representing the model with and without the i transition through the Anderson–Darling (AD) test.[9] In both cases the AD T statistic (0.01 and 0.41, respectively) is much lower than the critical value (0.697) and consequently, the hypothesis that both models represent the available data cannot be rejected. However, the latter statistic is much closer to the critical value than the former, meaning that the fit significantly improves when the line is included. In conclusion, the i transition appears to be significant but extremely faint.

We can quantitatively estimate the formation region of the Si XIII lines by comparing the observed f/i ratio $\mathcal{R}_{\rm obs}$ to the value $\mathcal{R}$ expected in the presence of the strong UV field of the donor star (Gabriel & Jordan 1969; Blumenthal et al. 1972; Waldron & Cassinelly 2007). Using the values quoted in Table 3 we obtain $\mathcal{R}_{\rm obs} = f/i = 2.4$, with a lower limit of $\mathcal{R}_{\rm obs} \geqslant 1.47$. In the absence of UV or X-ray sources in the vicinity of the emitting volume, and at a temperature where the emission from the Si XIII triplet peaks ($T \sim 5$ MK), the f/i line ratio is expected to be $\mathcal{R}_0 = 2.3$ (Porquet et al. 2001). However, the strong X-ray irradiation in our case affects the f/i ratio as well, and $\mathcal{R}_0$ becomes a function of the ionization fraction, electron density $n_{\rm e}$ and electron temperature T. Porquet & Dubau (2000) calculated values for $\mathcal{R}_0(T, n_{\rm e})$ assuming different ionization fractions. In the case of dominant X-ray irradiation, which is appropriate here, and assuming $n_{\rm e} \lesssim 10^{12}$ cm^{-3} and $T \sim 5$ MK, the expected f/i ratio is $\mathcal{R}_0 \sim 2.7$ (Porquet & Dubau 2000; see. Figure 8). Densities larger than 10^{12} cm^{-3} would imply unrealistic clumping contrasts of the order of 1000, while assuming the peak Si XIII temperature of $T \sim 5$ MK is further supported by the observed $\mathcal{G} = (i + f)/r$ ratio of ~1 (Porquet & Dubau 2000; see Figure 7). Although this is a rough estimate, the conclusions given below are not strongly sensible to the exact value of $\mathcal{R}_0$.

To obtain the donor's UV field, we calculate a model with typical parameters for an B0 supergiant using the Potsdam Wolf–Rayet (PoWR) code, which is applicable for any hot star with expanding atmosphere (Hamann & Gräfener 2004). Based on the discussion above, we assume $R_0 = 2.7$. In Figure 8, we compare the expected value of $\mathcal{R}(r)$ in the presence of this UV field with the observed lower limit for the system. Note that we assume here a localized formation region; the results obtained assuming extended formation regions (Leutenegger et al. 2006) are similar. The results imply that the corresponding X-ray formation regions are located at distances $r_{\rm min} \gtrsim 1.1\ R_*$ above the photosphere of the donor, and would suggest an average formation radius of $r \sim 2\ R_*$. The wind speed at this distance is ~1300 km s^{-1} and the expected broadening $\Delta\lambda \approx 0.03$ Å, roughly six times the observed value. Therefore the Si XIII triplet must be produced fairly close the star.

4.2.2. The Si XIV and Mg XII Lyα Lines

The Si XIV Lyα transition at 6.1880 Å can be clearly seen both out and during eclipse, showing the same intensity in both phases (see Figure 5). Therefore it is produced at radial

[9] http://asaip.psu.edu/Articles/beware-the-kolmogorov-smirnov-test

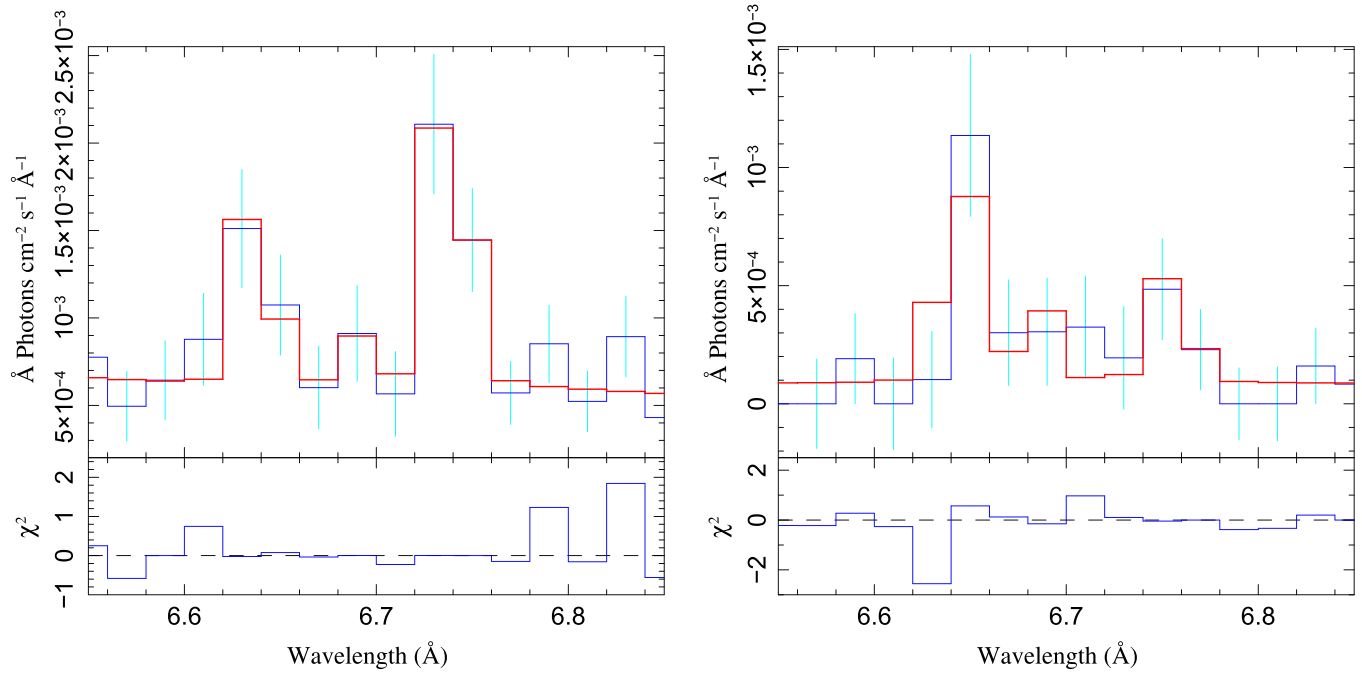

Figure 6. Si XIII He-like triplet out of eclipse (left) and during eclipse (right). The intercombination transition i is clearly suppressed. Out of eclipse $r < f$, while in eclipse $r > f$, which might be due to resonant scattering in the wind.

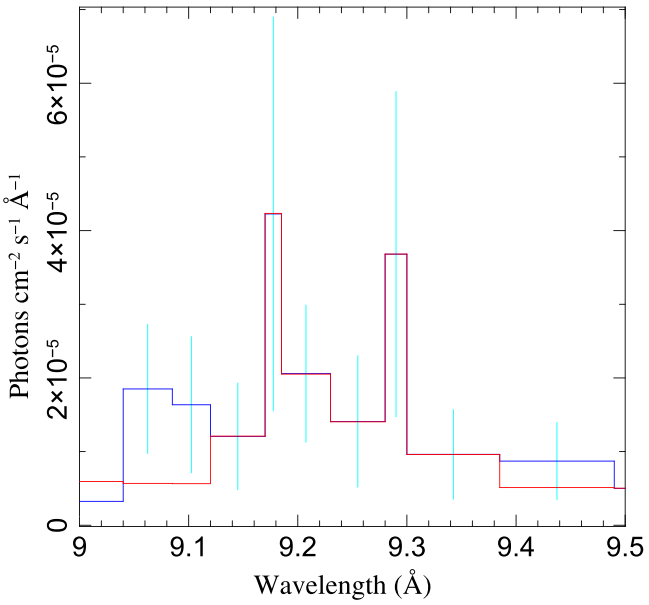

Figure 7. Mg XI He-like triplet out of eclipse. As with the Si XIII line, the intercombination transition i is present but very weak.

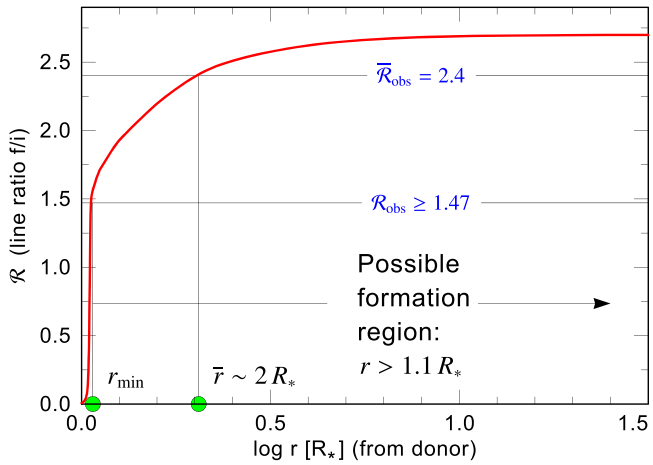

Figure 8. Theoretical f/i ratio $\mathcal{R}(r)$ as a function of the X-ray formation radius (red solid line) for the Si XIII ion. The intersection of the measured lower limit with $\mathcal{R}(r)$ implies a minimum formation radius of $r_{min} \approx 1.1R_*$. Likewise, the observed value $\bar{\mathcal{R}}$ implies a typical formation radius of about $2R_*$. An upper limit of the f/i ratio, and hence of the formation region of Si XIII, cannot be constrained with the data at hand (see Table 3).

distances from the NS larger than $r_X > 1R_*$, so that the production site is not eclipsed, or it is effectively resonantly scattered into the observer's line of sight by the wind. This line can be used to estimate the mass-loss rate of the donor using the calculations of Watanabe et al. (2006; Figure 15 of this reference, right panel) assuming that the average wind properties of Vela X-1 and QV Nor are essentially the same. From the fluxes quoted in Table 3 we roughly estimate a mass-loss rate of $\dot{M}_* = [0.2, 2.1] \times 10^{-6} M_\odot\,\mathrm{yr}^{-1}$. This is in agreement with the PoWR models.

The Mg XII Lyα transition ($\lambda = 8.4236$ Å) is the strongest found in the spectrum of QV Nor. It is marginally resolved with a width of $\sigma = 0.009^{+0.009}_{-0.005}$ Å. This sets an upper limit for the bulk plasma velocity of 640 km s^{-1}.

4.2.3. The Fe Lines

Contrary to the Si and Mg lines, the Fe lines do show significant differences both in and out of eclipse. Consequently, we have performed the fitting separately for the different orbital phases and the corresponding parameters are presented in Table 4. In Figure 9 we show the 1.65–2.2 Å region. The fluorescence Kα and Kβ lines of near-neutral Fe are clearly seen together with the Fe XXV He-like transition and the Fe K edge at 1.705 Å. No Fe XXVI H-like (at 1.7807 Å) seems to be

Table 4
Fe Emission Lines Identified in the *Chandra* Spectrum of QV Nor at Several Orbital Phases

Ion	λ (Å)	Flux $\times 10^{-4}$ (ph s^{-1} cm^{-2})	σ (Å)
	Out of Eclipse		
Fe Kβ	$1.7551^{+0.0035}_{-0.0021}$	$0.5^{+0.1}_{-0.4}$	$\leqslant$0.005
Fe XXV	1.8588 ± 0.0025	$0.5^{+0.4}_{-0.4}$	$\leqslant$0.005
Fe Kα	$1.9368^{+0.0032}_{-0.0018}$	$1.4^{+0.3}_{-0.1}$	$\leqslant$0.005
	Eclipse		
Fe Kβ	$1.7551^{+0.0036}_{-0.0021}$	$0.22^{+0.6}_{-0.15}$	0.005
Fe XXV	1.8574 ± 0.0025	$0.3^{+0.7}_{-0.2}$	0.005
Fe Kα	$1.9368^{+0.0035}_{-0.0019}$	0.38 ± 0.16	0.005

Note. Numbers without errors are fixed to the quoted value.

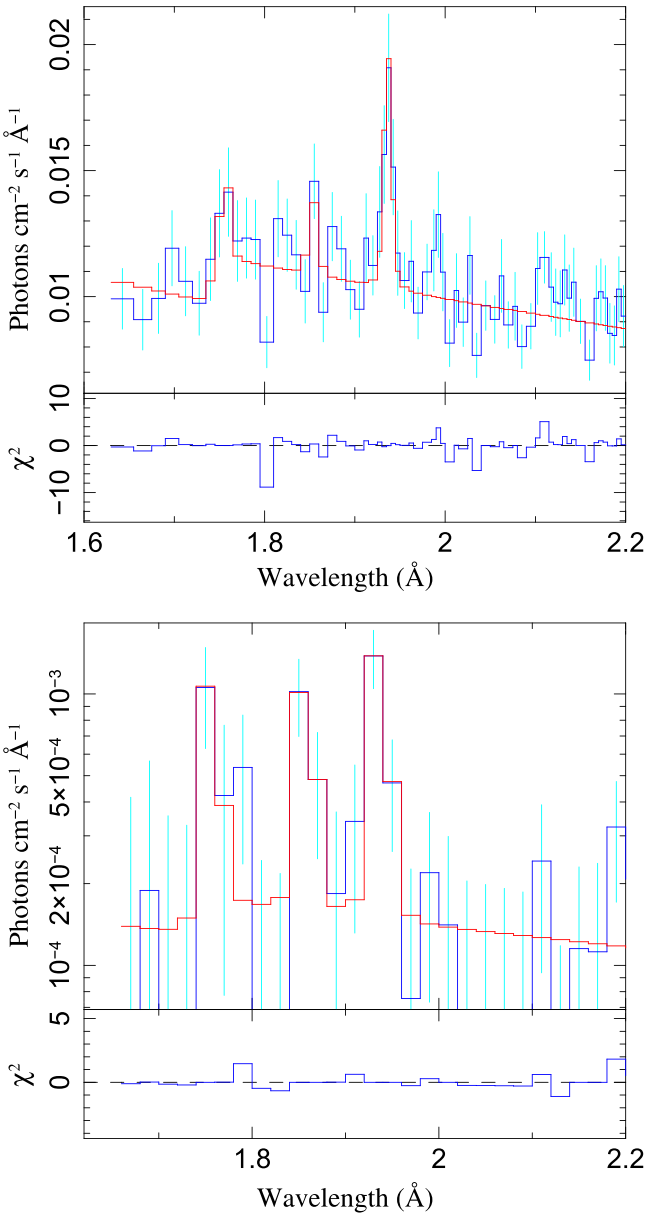

Figure 9. Top: Fe Kα line out of eclipse. Bottom: same line during eclipse.

present. Likewise, no Fe lines are detected at all in the ingress (*I*) spectrum.

The winds of hot stars are accelerating outward and the mechanisms of formation of X-ray emission lines in such winds are well understood (Ignace 2001; Oskinova et al. 2006). The line profile shapes may strongly depart from a simple Gaussian profile and provide a wealth of information on wind structure, especially for the lines formed at the softest parts of the X-ray spectrum (Hervé et al. 2012). On the other hand, the cool portion of the stellar wind is essentially transparent for the X-rays at the wavelength Fe Kα line ($\lambda \simeq 1.94$ Å Oskinova et al. 2006; Hervé et al. 2012). Therefore, for simplicity we formally fit them with a Gaussian component to obtain a fiducial characterization of line broadening. A quantitative analysis yields the following conclusions.

1. The observed wavelength of the Fe Kα line is $\lambda_{\mathrm{FeK}\alpha} = 1.9368^{+0.0032}_{-0.0018}$ Å, within the range of the majority of HMXBs observed at a high resolution (Torrejón et al. 2010). The ionization degree implied that this wavelength range is Fe II-X.[10] The most abundant ion inferred from the central wavelength must be Fe III-VIII. This is consistent with the fact that the leading ion in B0I star winds, inferred from optical-UV, is Fe IV (Giménez-García et al. 2015). Therefore, the Fe Kα line is tracing material with ionization parameters in the range $\log \xi \in [-1, 2]$ (Kallman et al. 2004, Figure 5) with a most likely predominance of $\log \xi \leqslant 0$.
2. The line width is not resolved even at *Chandra* HEG gratings spectral resolution, which puts a limit on the $\sigma_{\mathrm{Fe\ K}\alpha} \leqslant 0.005$ Å, corresponding to $\approx$800 km s^{-1}. This means that the bulk of the material emitting X-rays at the Fe Kα wavelength is not moving at velocities higher than this.
3. The flux of the Fe Kα line during eclipse is $\sim(30 \pm 15)\%$ of the line flux out-of-eclipse.

5. DISCUSSION

The eclipse spectrum shows a continuum with a flux reduced to $\sim$3% of the flux out-of-eclipse. This is expected since the source of the continuum is completely blocked from view and we only observe the continuum (with the same shape) scattered into the observer direction by the stellar wind. In the out-of-eclipse spectrum, the equivalent width of the Fe Kα line is 37 eV, which implies a reprocessing region with a density column $N_{\mathrm{H}} \approx 10 \times 10^{22}$ cm^{-2} (Torrejón et al. 2010). This is of the order of the local N_{H}^2 (Table 2) and therefore compatible with the stellar wind of the donor as the primary site of Fe fluorescence.

Contrary to the behavior of the *r* transition in the He-like Si triplet, the Fe Kα photons cannot be resonantly scattered in the wind. Indeed, Kα photons produced in an eclipsed area cannot excite fluorescence in other regions because they do not have the required energy: only photons with wavelengths that are shortward of the Fe K edge ($\lambda < 1.75$ Å) can effectively excite fluorescence. In other words, all of the Fe Kα photons we observe must come from regions directly in the line of sight toward the observer and toward the NS *simultaneously*.

[10] XSTAR http://heasarc.gsfc.nasa.gov/docs/software/xstar/xstar.html

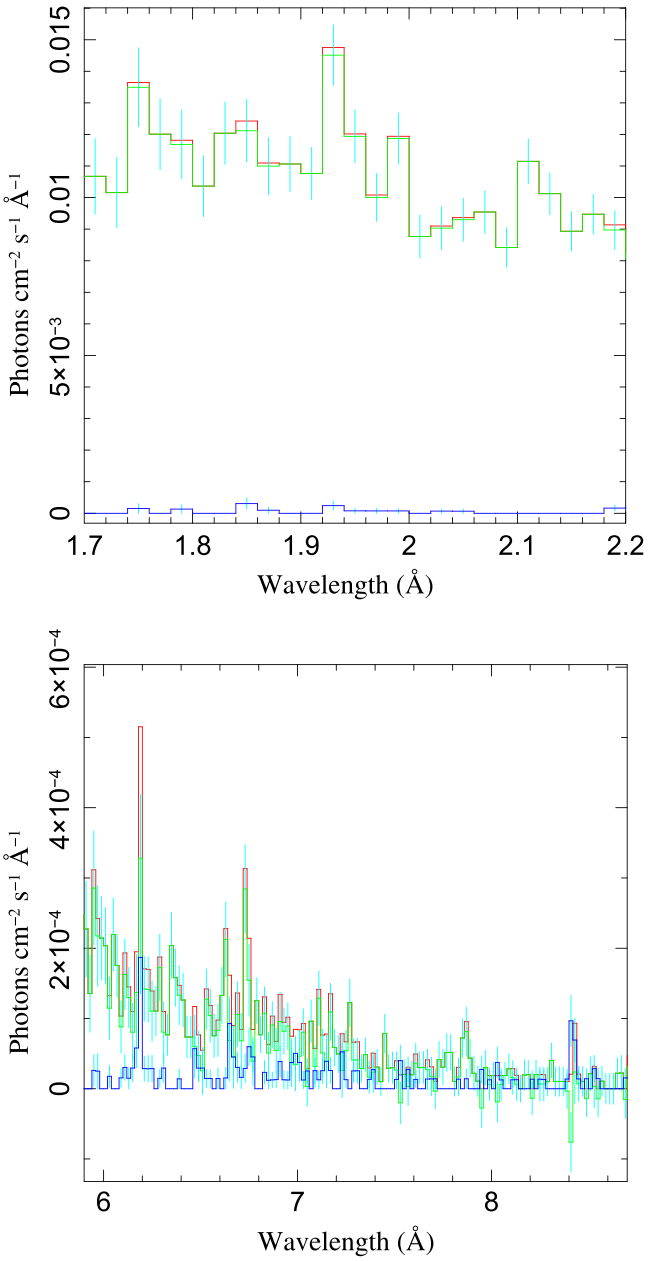

Figure 10. Top: Fe Kα region showing the out-of-eclipse spectrum (red), the eclipse spectrum (blue, barely visible at the bottom of the plot) and the subtracted spectrum (green). As can be seen, the contribution of the eclipse spectrum to the total spectrum is very small. The errors are only shown for the eclipse and subtracted spectrum for clarity. Bottom: 5.9–8.7 Å region with the same color code as before.

The Fe Kα emission decreases to ~30% of the flux out-of-eclipse. This implies that a substantial amount of Fe Kα emission must be produced at distances from the NS larger than $r_X > 1R_*$ (we only see fluorescence from regions in the line of sight). On the other hand, the majority of the emission (~70%) must be produced at distances $r_X < 1R_*$ from the NS. It is only due to the fact that the intensity of the continuum decreases much more during the eclipse compared with the line that we can observe the emission (in an effect similar to the Solar corona during the Solar eclipses). In an attempt to isolate the spectrum of the regions closer to the NS, we have subtracted the eclipse spectrum (produced in the farther regions) from the out-of-eclipse spectrum. In Figure 10 we present the subtracted spectrum (green) together with the combined (red) and the eclipse spectra (blue). As can be seen (left panel) the contribution of the farther reprocessing regions to the total fluorescence line is very small.

We have found that Fe Kα is narrow. The bulk of the stellar wind where it is produced must be moving at speeds lower than ~800 km s^{-1}. In the left panel of Figure 11 we have plotted some contours of constant ionization for the wind density profile deduced by CWN94 (the star itself has a radius of 0.97×10^{12} cm), considering a homogeneous wind. These contours are overlaid on the color-coded wind velocity. The Fe Kα reprocessing region is constrained to be below wind speeds of 800 km s^{-1}, marked with a blue open circle. On the other hand, the ionization parameter must be low to keep the ionized species below Fe X (mostly below Fe VIII). The Fe Kα production site must reside below ("leftwards" in the plot) of the $\log \xi = 2$ contour line.

In the right panel of Figure 11 we plot the same parameters for a clumped wind. As stated in Oskinova et al. (2012), in a medium with density fluctuations, the number of recombinations (proportional to the density squared) is enhanced with respect to the number of ionizations (proportional to the density). Consequently the ionization parameter is reduced in a clumped wind by a factor f_v^{-1}, where f_v is the volume filling factor, defined as the fraction of total wind volume that is filled by clumps . We use $f_v = 0.1$, typical for OB stars. The effect is to allow the Fe Kα photons to be produced closer to the NS. However, this does not affect the line width, which still constrains it relatively close to the stellar surface.

The intersection volume between the constant ionization surface and the constant velocity surface (around 800 km s^{-1}) is from where the Fe Kα emission must come. As can be seen, the observed Fe Kα fluorescence must be produced at radial distances from QV Nor below $r \sim 1.25R_*$. At this distance, the particle number density given by CWN94 (Equation (2.4)) for QV Nor is $n \approx 2 \times 10^{10}$ cm^{-3}. On the other hand, in order to have Fe Kα fluorescence from near-neutral Fe we need to meet the condition $nr_X^2 \leqslant 10^{34}$ cm^{-1}. For $r = 1.25R_*$ ($r_X = 0.15R_*$), we then need $n \approx 10^{11}$ cm^{-3}, that is, an overdensity of a factor of 10 higher than the average given by the smooth wind approximation. Therefore, the wind must be significantly clumped at radial distances $r \sim 1.25R_*$. On the other hand, if the mass-loss rate were sufficiently large ($\dot{M} \geqslant 10^{-6} M_\odot$ yr^{-1}), the particle density could be high enough that even a smooth wind could produce Fe Kα fluorescence at such small radial distances. CWN94 deduce a mass-loss for QV Nor in the range $(0.9–1.9) \times 10^{-6} M_\odot$ yr^{-1}, compatible with our own estimation, and hence on the fringe of this condition. However, the high variability seen in the light curve would not be expected in a smooth wind.

In Figure 12 we plot a simplified (not to scale) sketch of the homogeneous wind scenario in two orbital phases. The regions marked with the letters *f* and *F* are where the line is produced. The two regions marked with *f* are the only ones that can be observed during eclipse but these only contribute 30% of the flux. The other 70% must come from the region *F* that is close to the stellar surface of QV Nor , in the direction facing the NS.

In this scenario, during eclipse ingress (*I*) the X-ray illuminated face of the donor star *F* is hidden from view (see Figure 12, right panel), as it is during the eclipse. But now one of the lobes where the "distant" Kα photons originate is also

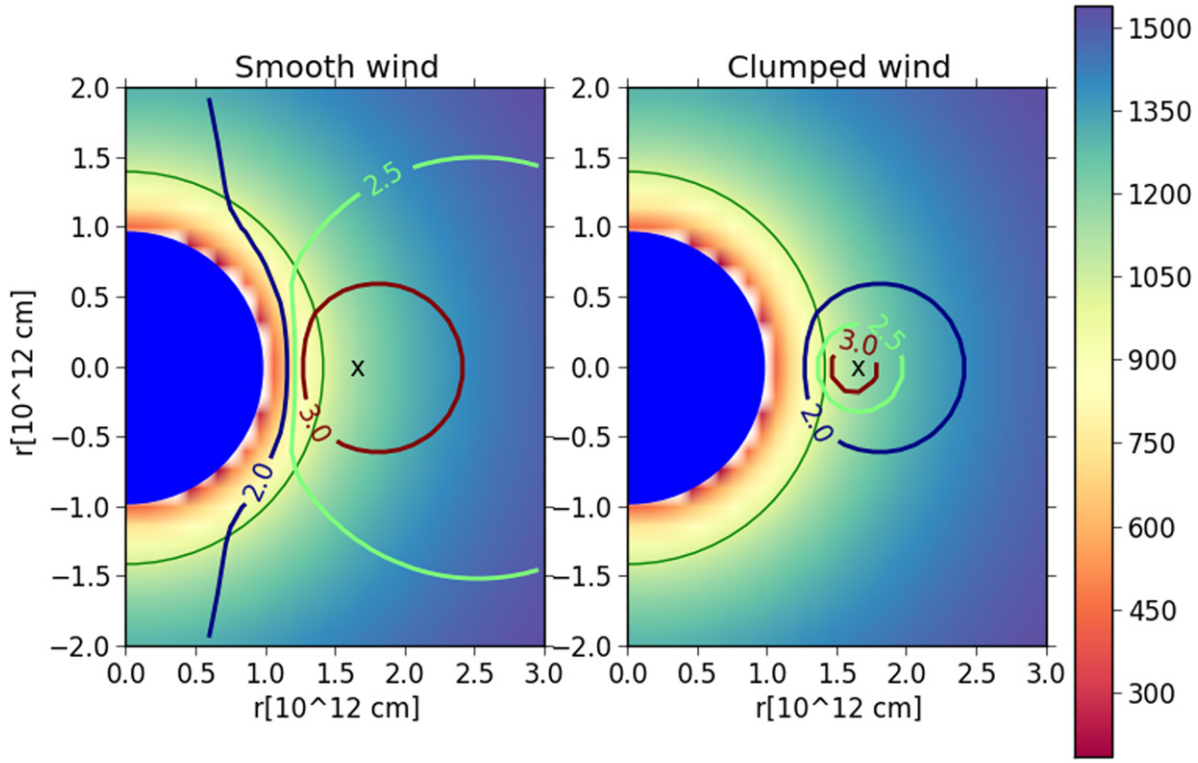

Figure 11. Contour plots of constant log ξ values for the cases of smooth wind (left, corresponding to Figure 8 in CWN94) and clumped wind (right). The bar in the right panel shows the color-coded range of wind speed values in km s^{-1} for $v_\infty = 1800$ km s^{-1} and $\beta = 0.5$. The "x" at three o'clock marks the position of the neutron star. The filled blue circle is the stellar core and the open green circle marks the limit of 800 km s^{-1} wind speed. The intersection of the volumes for which log $\xi \leqslant 2$ and $v_w \leqslant 800$ km s^{-1} is the Fe Kα reprocessing region.

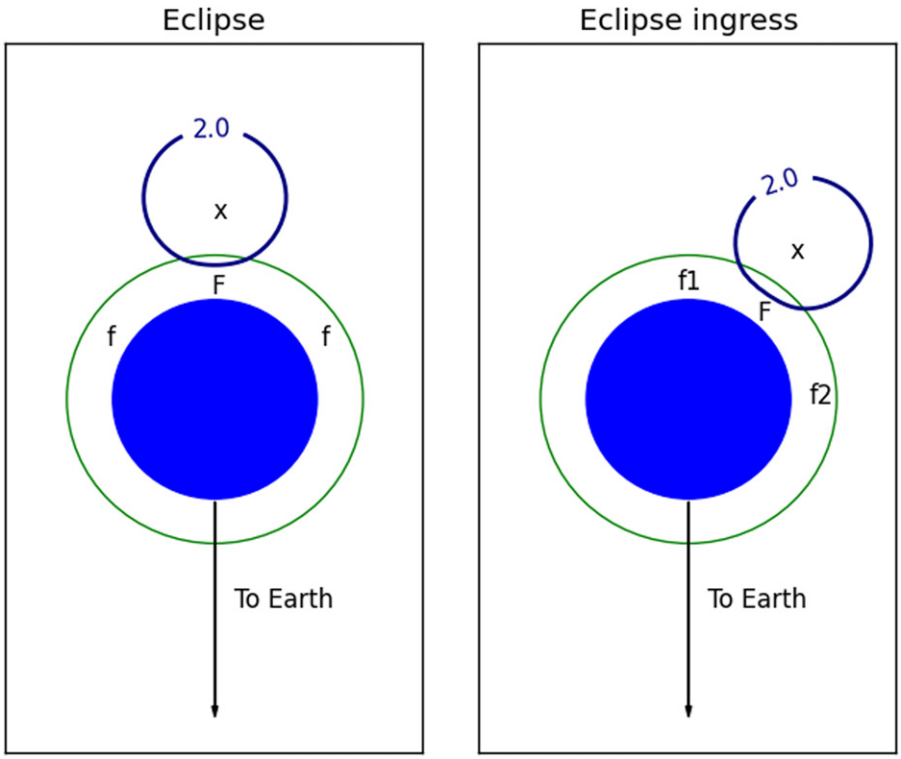

Figure 12. Sketch (not to scale) of the system in two orbital phases, eclipse (*E*) in the left panel and eclipse ingress (*I*) in the right panel. Only the constant log $\xi = 2.0$ curve for the clumped wind scenario is plotted for clarity. The green circle marks the limit of wind speed below 800 km s^{-1}. The Fe Kα emitting areas must be inside the intersection between these two conditions and are marked with the *f* and *F* signs. The *f* areas are the only ones seen during eclipse, while the *F* area, close to the surface of the star, is the one characterized by the subtracted spectrum presented in this paper. During eclipse ingress (right panel) the *F* region and one of the *f* regions (here marked as *f*1) are eclipsed, leading to a minimum Fe Kα emission.

eclipsed (marked here as *f*1), at least partially. Then the Fe Kα total emission should be even lower in phase *I* than during eclipse *E*. Some evidence exists in this direction. On one hand the spectrum of bin *I* shows no Fe lines even though the Fe Kα line is the strongest one and should be detectable. On the other hand, if this scenario is correct, the maximum Fe Kα emission should be observable at orbital phase $\phi = 0.5$ when we see the region *F* face on, as well as the "distant" reprocessing region. This effect can be seen clearly in CWN94 (Figure 2, middle panel).

Two other regions can meet the conditions of high density and/or low velocity. In the accretion wake the density is also higher than average. Any fluorescence coming from the accretion wake must be a minor contribution to the total emission, nevertheless, because this extended structure would still be clearly visible in a phase bin *I* where no Fe Kα line is observed. On the other hand, the low-velocity constraint can also be met by the ionization wake. Indeed, the stellar wind is photoionized by the X-rays of the NS, thereby hindering the wind acceleration in the NS vicinity (typically when $\log \xi \geqslant 3$).This creates an area of low velocity, stalled wind trailing the NS against which the accelerated—non-ionized—wind collides, producing the so-called ionization wake. However, the possible contribution of this wake to the Fe Kα emission must be minor because the Fe Kα fluorescence comes from near-neutral iron.

6. CONCLUSIONS

The stellar wind of the B0I star QV Nor must be significantly clumped at radial distances $r < 1.25R_*$ in the wind regions that meet the constraints: (a) wind ionization parameter $\log \xi \leqslant 2$ and (b) wind velocity $v_w \leqslant 800\ \mathrm{km\ s^{-1}}$. Given that both values are upper limits, the Fe Kα emission is probably coming from regions even closer to the photosphere of the star, mostly in the hemisphere that faces the NS. At such small radial distances, the wind instabilities may not be yet fully developed and there may be a need to invoke a triggering mechanism at the photosphere. Cantiello & Braithwaite (2011) have suggested that sub-surface convection can be at work in the photosphere of hot massive stars, giving rise to localized surface magnetic fields. This mechanism could play a role in triggering clump formation that is already at the stellar photosphere. We conclude that the new *Chandra* observations of the X-ray binary QV Nor , using the orbiting NS as a probe of the inner stellar wind, provide firm empirical evidence of strong inhomogeneity of the B-type supergiant wind close to the stellar photosphere.

We acknowledge the anonymous referee, whose constructive criticism helped to improve the paper. This work has been supported by the Ministerio de Economía y Competitividad (MINECO) through grants ESP2013-48637-C2-2P and ESP2014-53672-C3-3-P. J.J.R.R. acknowledges support by the Vicerectorat d'Investigació, Desenvolupament i Innovació de la Universitat d'Alacant project number GRE12-35, and by the Generalitat Valenciana project number GV2014/088.

REFERENCES

Baykal, A., Inam, S., & Beklen, E. 2006, A&A, 453, 1037
Blumenthal, G. R., Drake, G. W. F., & Tucker, W. H. 1972, ApJ, 172, 205
Bouret, J. C., Lanz, T., & Hillier, D. J. 2005, A&A, 438, 301
Canizares, C., Davis, J. E., Dewey, D., et al. 2005, PASP, 117, 1144
Cantiello, M., & Braithwaite, J. 2011, A&A, 534, A140
Castor, J. I., Abbott, D. C., & Klein, R. I. 1975, ApJ, 195, 157
Clark, G. W. 2000, ApJL, 542, L131
Clark, G. W., Woo, J. W., & Nagase, F. 1994, ApJ, 422, 336
Crampton, D., Hutchings, J. B., & Cowley, A. P. 1978, ApJL, 225, L63
Ebbets, D. 1982, ApJS, 48, 399
Eversberg, T., Lépine, S., Moffat, A. F. J., et al. 1998, ApJ, 494, 799
Feldmeier, A. 1995, A&A, 299, 523
Feldmeier, A., Puls, J., & Pauldrach, A. W. A. 1997, A&A, 322, 878
Fullerton, A. W., Massa, D. L., Prinja, R. K., et al. 2006, ApJ, 637, 1025
Gabriel, A. H., & Jordan, C. 1969, MNRAS, 145, 241
Giménez-García, A., Torrejón, J. M., Eikmann, W., et al. 2015, A&A, 576, 108
Hamann, W. R., & Gräfener, G.2004, A&A, 427, 697
Hamann, W. R., Oskinova, L., & Feldmeier, A. (ed.) 2008, Clumping Hot Star Winds (Potsdam: Univ. Verl.)
Hemphill, P. B., Rothschild, R. E., Markowitz, A., et al. 2014, ApJ, 792, 14
Hervé, Rauw, G., Nazé, Y., & Foster, A. 2012, ApJ, 748, 89
Hickox, R. C., Narayan, R., & Kallman, T. R. 2004, ApJ, 614, 881
Houck, J. C., & Denicola, L. A. 2000, in ASP Conf. Ser. 9, Astronomical Data Analysis Software and Systems IX , ed. N. Manset, C. Veillet & D. Crabtree (San Francisco, CA: ASP), 591
Ignace, R. 2001, ApJ, 549, 119
Kallman, T. R., Palmeri, P., Bautista, M. A., Mendoza, C., & Krolik, J. H. 2004, ApJS, 155, 675
Kaper, L., Henrichs, H. F., Nichols, J. S., et al. 1996, A&AS, 116, 257
Leutenegger, M. A., Paerels, F. B. S, Kahn, S. M., & Cohen, D. H. 2006, ApJ, 650, 1096
Lépine, S., & Moffat, A. F. J., 2008, AJ, 136, 548
Lucy, L. B., & Solomon, P. M. 1970, ApJ, 159, 879
Lucy, L. B., & White, R. L. 1980, ApJ, 241, 300
MacGregor, K. B., Hartmann, L., & Raymond, J. C. 1979, ApJ, 231, 514
Martínez-Núñez, S., Torrejón, J. M., Kühnel, M., et al. 2014, A&A, 563, A70
Massa, D., Fullerton, A. W., Sonneborn, G., & Hutchings, J. B. 2003, ApJ, 586, 996
Mukherjee, U., Raichur, H., Paul, B., Naik, S., & Bhatt, N. 2006, JApA, 27, 411
Oskinova, L. M., Feldmeier, A., Hamann, & W.-R.2004, A&A, 422, 675
Oskinova, L. M., Feldmeier, A., & Hamann, W.-R. 2006, MNRAS, 372, 313
Oskinova, L. M., Hamann, W.-R., & Feldmeier, A. 2007, A&A, 476, 1331
Oskinova, L. M., Feldmeier, A., & Kretschmar, P. 2012, MNRAS, 421, 2820
Owocki, S. P., Castor, J. I., & Rybicki, G. B. 1988, ApJ, 335, 914
Porquet, D., & Dubau, J. 2000, A&AS, 143, 495
Porquet, D., Mewe, R., Dubau, J., Raasen, A. J., & Kaastra, J. S. 2001, A&A, 376, 1113
Prinja, R. K., & Massa, D. L. 2010, A&A, 521, 55
Prinja, & Massa 2013, A&A, 559, 15
Puls, J., Markova, N., Scuderi, S., et al. 2006, A&A, 454, 625
Rawls, M. L., Orosz, J. A., McClintock, J. E., et al. 2011, ApJ, 730, 25
Reynolds, A. P., Bell, S. A., & Hilditch, R. W. 1992, MNRAS, 256, 631
Rodes-Roca, J. J., Mihara, T., Nakahira, S., et al. 2015, A&A, 580, A140
Rodes-Roca, J. J., Page, K. L., Torrejón, J. M., Osborne, J. P., & Bernabéu, G. 2011, A&A, 526, A64
Schulz, N. S., Canizares, C. R., Lee, J. C., & Sako, M. 2002, ApJL, 564, L21
Shenar, T., Oskinova, L., Hamann, W.-R, et al. 2015, ApJ, 809, 135
Šurlan, Hamann, W.-R., Aret, A., et al. 2013, A&A, 559, 130
Torrejón, J. M., Schulz, N. S., Nowak, M. A., & Kallman, T. 2010, ApJ, 715, 947
Verner, D. A., Ferland, G. J., Korista, K. T., & Yakovlev, D. G. 1996, ApJ, 465, 487
Waldron, W. L., & Cassinelly, J. P. 2007, ApJ, 668, 456
Watanabe, S., Sako, M., Ishida, M., et al. 2006, ApJ, 651m, 421
Wilms, J., Allen, A., & McKray, R. 2000, ApJ, 542, 914
Wilms, J., Lee, J. C., Nowak, M. A., et al. 2010, BAAS, 42, 674
Zsargó, J., Hillier, D. J., Bouret, J.-C., et al. 2008, ApJ, 685L, 149